Pergamon

Int. J. Heat Mass Transfer. Vol. 41, Nos 4–5, pp. 785–796, 1998

Printed in Great Britain
0017–9310/98 $19.00+0.00

PII: S0017–9310(97)00128–2

Heat transfer in Rayleigh–Bénard convection with air in moderate size containers

J. G. MAVEETY

Intel Corporation, Santa Clara Validation Center, M/S: SC9-32, 2200 Mission College Blvd, Santa Clara, CA 95052, U.S.A.

and

J. R. LEITH†

Department of Mechanical Engineering, The University of New Mexico, Albuquerque, NM 87131, U.S.A.

(*Received* 27 *September* 1996 *and in final form* 25 *April* 1997)

Abstract—The work presented here concerns a class of problems in thermal convection in which the mechanisms responsible for the evolution of a dynamical system to different states of self-organization are explored. Experimental investigations of the wavenumber and heat flux characteristics for Rayleigh–Bénard convection in moderate size containers with air exhibit a secondary bifurcation structure which can be understood, in the hierarchical sense, in terms of the behavior in families of container size as specified by the primary aspect ratio, L/d. It is concluded that the heat transport is strongly dependent on both size and shape of the container. For the work presented here, the near onset quadratic growth rate of heat flux is shown to relax to that of a linear growth rate in containers with increasing primary aspect ratio. The linear growth in heat flux has been previously obtained from experiments in extended systems, and the theoretical results obtained by considering low amplitude convection in extended systems. © 1997 Elsevier Science Ltd.

1. INTRODUCTION

Buoyancy-driven thermal convection resulting from the heating of a lower surface and the cooling of an upper surface is an important mechanism of heat and mass transfer in geophysical and astrophysical phenomena, as well as technological devices such as solar collectors and energy storage systems such as batteries. There are many cases in which the effects of buoyancy and density difference induced flows cannot be ignored. These interactions lead to interesting flow and stability problems. Only recently has the importance of the effects of natural convection on the growth of a pure crystal in micro-gravity been initiated. It has been established that natural convection develops in the crystal melt, and greatly affects the rate of melting, the shape of the crystal and, consequently, the purity of the crystal. The critical issues concerning buoyancy induced flows range from understanding the physical phenomena, to verifying methods of analysis.

Rayleigh–Bénard convection concerns the stability of horizontal fluid layers heated below and cooled above. Whereas much is known of the hydrodynamic stability characteristics of Rayleigh–Bénard convection in laterally large fluid layers [1, 2], our knowledge is most incomplete concerning the instability mechanisms as they are modulated by the presence of vertical boundaries. The parameters used to describe these processes are usually expressed as dimensionless groups, with the Rayleigh number (Ra) and Prandtl number (Pr) specifying the buoyant force and the fluid type, respectively, and the wavenumber (a) as an inverse function of the dominant length scale of the convection.

2. PHYSICS OF THE RAYLEIGH–BÉNARD PROBLEM

The dimensionless number typifying the ratio of the destabilising buoyancy force to the stabilizing diffusive force is termed the Rayleigh number $[Ra = (g\beta/\nu\alpha)d^3\Delta T]$, where g is the gravitational constant, β, ν and α are the coefficient of thermal expansion, kinematic viscosity and thermal diffusivity, respectively, d is the depth of the container and ΔT is the temperature difference between the upper and lower surfaces of the container. The Rayleigh number which signifies convective onset is called the *critical Rayleigh number* (Ra_c).

The low Rayleigh number behavior of Raleigh–Bénard convection is characterised by successive secondary bifurcations. Following the primary bifur-

† Author to whom correspondence should be addressed.

NOMENCLATURE

A	dimensionless amplitude
A, B	regression coefficients
a	wavenumber $[2\pi d/\lambda]$
a, b	regression coefficients
d	cell height [m]
H	heating rate [min]
L	cell length [m]
N	normalised dimensionless heat transfer
Nu	Nusselt number $[q_{conv}/q_{cond}]$
n	number of convection rolls
Pr	Prandtl number $[\nu/\alpha]$
q	heat flux [W m^{-2}]
R	thermal resistance [°C m^2 W^{-1}]
r	control parameter, equation (17)
Ra	Rayleigh number $[g\beta d^3 \Delta T/\nu\alpha]$
T	temperature [°C]
V	voltage [μV]
w	cell width [m].

Greek symbols

α	thermal diffusivity [m^2 s^{-1}]
β	coefficient of thermal expansion [K^{-1}]
ΔT	temperature difference [°C]
Δx	thickness of balsa substrate [m]
ζ	dimensionless control parameter $[Ra/Ra_c - 1]$
λ	wavelength-width of a roll pair
μ	absolute viscosity [kg m^{-1} s^{-1}]
ν	kinematic viscosity [m^2 s^{-1}]
ξ	dimensionless coherence length scale
ρ	density [kg m^{-3}]
τ	time constant [s].

Subscripts

c	cell when used with temperature difference, and critical when used with the Rayleigh number or wavenumber
cond	conduction
conv	convection
i	indexing of heat flux gauges
m	mean cell value.

cation at convective onset in a rectangular container, a stable non-oscillating, two-dimensional pattern comprised of co-rotating convection rolls aligned parallel to the short sidewalls is produced. Secondary bifurcations are comprised of the loss of a roll or roll pair with increasing buoyancy. The resulting wavenumber reduction is attributed to the skewed varicose instability, which induces spatially periodic contraction and dilation of convection rolls. The skewed varicose instability originates from the interaction of the nonlinear terms $u(\nabla \cdot u)$, $u(\nabla \cdot T)$ in the equations of motion and the energy equation. Growth of the skewed varicose instability is accompanied by macroscale dislocations, which nucleate at pinches in the rolls and exhibit a dynamical behavior in both climb and glide (motions parallel and transverse to the roll axis). Skewed varicose instability drives wavenumber reduction in the moderate size container regime with air, but the instability mechanism is strongly modulated by the close proximity of sidewalls. The net effect of reducing the container size in this regime is that stable patterns exist at higher buoyant force than in large containers, and this modulation effect becomes more pronounced with decreasing container size. Moreover, wavenumber reduction is limited by approximately a factor of two, so that the dynamical events of wavenumber reduction are of increasing magnitude for smaller containers [3]. Consequently, the finite Rayleigh–Bénard problem with gases exhibits a size-dependent bifurcation structure. The interest in air as a working fluid is that the secondary bifurcation structure induced by skewed varicose instability extends over a large range of buoyant force prior to the onset of oscillatory convection. It is then practical to investigate the stability of two-dimensional structure to three-dimensional disturbances (the skewed varicose instability), as modulated by container size and shape.

Our previous studies in the mechanism involved with the annihilation of convection rolls [3, 4] show that a dislocation nucleates at a roll intersection near a short sidewall and at a container corner, and this localised feature of defect nucleation is exhibited in containers with secondary aspect ratio, $w/L < 0.4$. Following defect nucleation and with imposed increase in the buoyant force, the dislocation moves parallel to the short sidewall (a climbing dynamical motion). Destruction of the defect at the opposite long sidewall then produces the net loss of a convection roll or roll pair. (In several experiments at constant buoyant force, it has been possible to induce roll annihilation at one end of the container and followed by roll nucleation at the opposite end of the container. The dynamical features repeat in both periodic and aperiodic sequence ($n \rightarrow n-1 \rightarrow n \ldots$), and this creates a physical realization of a *limit cycle*. An *alternate limit cycle* ($n \rightarrow n-1 \rightarrow n \rightarrow \ldots$) can be induced at constant buoyant force, with successive annihilation and nucleation of the roll at only one end of the container. Such experiments are highly reproducible [5].) Secondary bifurcation in rectangular-like containers assumes two limiting forms: (1) a gradual transition from an n to $n-1$ roll configuration by highly three-dimensional contraction and eventual annihilation of the wall roll (a *soft-mode* transition); or (2) a rapid annihilation of the wall roll, by a climbing motion

of the dislocation (a *hard-mode* transition). The two limiting forms appear to be independent of the rate of change in buoyant force (the experiments are operated at *slow* linear increase of the buoyant force), and the dynamics are most definitely dependent upon the specific container geometry [3, 4].

Gliding dislocations are exhibited in square-like containers, $0.7 < w/L < 1$, and the defects also nucleate near the short sidewalls of the container. In addition to the climbing motion, gliding of a dislocation introduces the defect into the interior pattern. Motion of the defect is dominated by glide, but a small component of climb (a distance of the order of one or two roll diameters) is evident in smoke flow visualisation experiments [5]. Near $w/L \sim 0.5$–0.7 and $L/d > 8$, the *initial* secondary bifurcation is accommodated by dislocation climb and annihilation. Gliding dislocations typically nucleate at one end of the container, and the dynamical character is manifested by an eventual annihilation of the dislocation at the opposite container wall. At an arbitrary time and at constant buoyant force, initiation of the process is usually followed by the presence of more than one gliding dislocation in the pattern. A single direction is preferred for the dynamical motions (rather as the vertical roll of a picture tube), and the initiation of the defect typically originates at the *same* short sidewall as for the previous secondary bifurcation. At constant buoyant force, gliding dislocations assume an aperiodic dynamical character (we have previously referred to the aperiodic dynamics as *phase turbulence* [6], in the sense that there is a recognisable form of convection rolls but there is also an absence of a *stable* pattern). On increase of the buoyant force, wavenumber reduction is accommodated by a *net decrease* of *one defect nucleation event*. Finally, it is noted that in the *small container regime*, $L/d < 8$, defects in the form of dislocations become *embedded* in the pattern. Such patterns can assume stationary form over a relatively large range of buoyant force, and the dynamical behavior at wavenumber reduction is most dramatic.

The heat flux results reported here do not necessarily represent the *dynamics* of secondary bifurcation, but the results clearly show the change in behavior corresponding to the change in wavenumber. Accordingly, results are available for rectangular-like containers, in which the principal mechanism of wavenumber reduction with increased buoyant force is accommodated by the nucleation and annihilation of climbing dislocations.

3. HEAT TRANSFER TEST APPARATUS

A schematic of the heat transfer cell is shown in Fig. 1. Each heat transfer surface was constructed of a three-layer laminate comprised of a 15 mm thick paraffin-filled foamed aluminum slab with embedded aluminum tubes, 3.2 mm thick heat flux gauges and 0.8 mm thick aluminum plates which bound the air layer. The aluminum plates have been chrome-plated to minimize the radiation heat transfer effects.

Two 36-gauge copper–constantan thermocouples were attached to each aluminum sheet, and were used to determine the temperature difference, ΔT_c, across the air layer. Four differential thermocouples were installed in the air layer in the central vertical plane co-parallel to the long sidewalls, as illustrated by V_2 in Fig. 1. Signals produced by the intrusive sensors produced voltage–time histories which were utilized in post-test analysis.

In these studies, thin film heat flux gauges were constructed based upon the work developed by Hager [7]. This method consists of utilizing the Seebeck effect to obtain a recordable voltage by fusing two dissimilar metals together and forming a low-impedance differential thermocouple system which produces an *emf* proportional to the temperature difference across an insulator. The gauges were fabricated from 0.025 mm thick copper and nickel foils and were laminated to a 3.175 mm thick balsa-wood substrate. The foils were silver-soldered to form line thermojunctions at both horizontal surfaces of the balsa wood substrate. Thermojunctions of the gauges were consequently co-parallel to the long-side central vertical plane of the apparatus, so that the surface heat flux measurement is normal to the center-line cross-sections of the convection rolls. The gauges have a width of 40 mm and length of 100 mm, so that six gauges at both upper and lower surfaces were available for measurements.

The experimental errors in heat flux, as found in our earlier work, were determined to be within $\pm 5\%$ [4, 8]. In the design of the sensors, we have opted for signal strength at some loss to the dynamic response. The gauges produce a voltage at convective onset of about 10 μV, with measurement resolution from the HP-3456A voltmeter of 0.1 μV.

A series of 14 quasi-steady calibration experiments were conducted, with excursion time periods of 90–420 min to similar steady-state conditions. Figure 2 illustrates the positive relative error as a function of the offset of mean test cell operating temperature from the laboratory ambient temperature. The experimental data included in Fig. 2 were taken at random from five of the 14 experiments, which included a total of approximately 5000 time records of measurement. The relative error, $1 - V/V_{cal}$, is assumed as the relation between the measured voltage, V, and the least-squares generated voltage at the same cell temperature difference, V_{cal}. Of all attributes in our experiments, the strongest correlation of experimental error corresponds to a dependence of the offset temperature difference, $\phi - \phi_{cal}$ (with $\phi = \bar{T}_c - T_\infty$ and $\bar{T}_c$ as the constant mean cell temperature), Fig. 2. The condition $\phi - \phi_{cal} \to 0$ gives identically a *net adiabatic heat transfer interaction* between the test cell and laboratory ambient. Indeed, Fig. 2 shows experimental error below $\pm 5\%$ provided that the offset temperature difference is smaller than ± 0.05°C. Accordingly, the only heat flux results for the Rayleigh–Bénard exper-

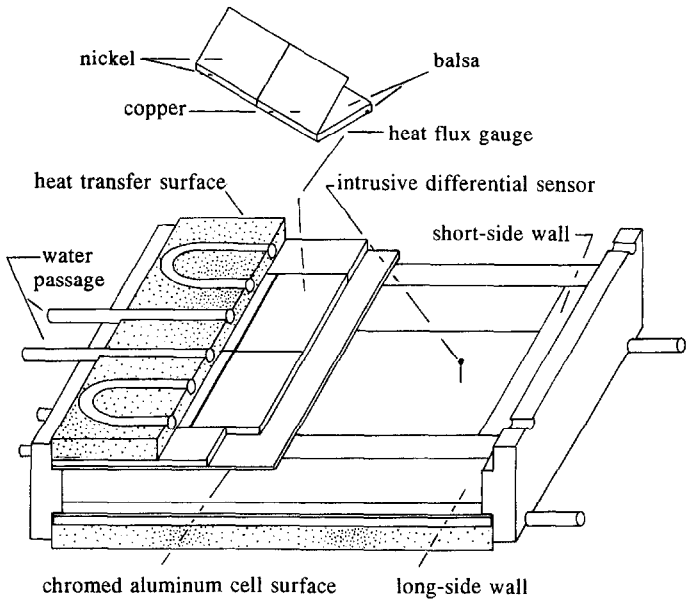

Fig. 1. Schematic of apparatus used in heat flux experiments.

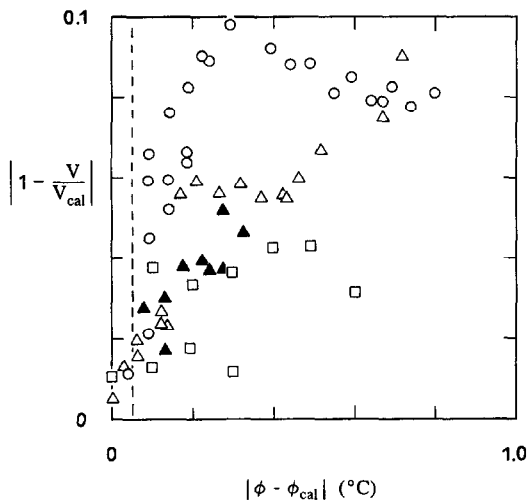

Fig. 2. Positive error in heat flux measurement for inner sensors, as taken at random from approximately 4000 time records in four conduction calibration experiments.

iments reported here are those measurements for which $|\phi - \phi_{cal}| < 0.05°C$. This stringent requirement for error qualification of our experimental data necessitated a total of 60 experiments for the five geometries considered below.

A comparison of experimental and numerical transient response of the heat flux gauges was performed in order to qualify gauge characteristics. Measurements of the thermal resistance of the gauges using both experimental values of temperature and voltage are $R_t = 0.217 \pm 0.005°C\ m^2\ W^{-1}$ and $R_t = 0.192 \pm 0.009°C\ m^2\ W^{-1}$, respectively [4, 8]. The thermal resistance of the gauges as determined from numerical simulation is $R_t = 0.209 \pm 0.009°C\ m^2\ W^{-1}$ [4, 8].

The numerical experiments allowed a sensitivity analysis of the thermophysical properties to determine 'optimum' properties of the heat flux gauges, as those which produce minimum error between the theoretical and experimental observed response of the gauges. The resulting study revealed that the balsa substrate is more sensitive to changes in thermal diffusivity than to changes in its heat capacity, ρc_p. This simply confirms that the roll of the balsa substrate is that of thermal resistance. Based on this analysis it was found that an approximation to the characteristics time from heat conduction [9], $\tau_{gauge} \simeq \Delta x^2/\alpha$ (with Δx = balsa thickness) as $\tau_{gauge} \simeq 100\ s \pm 3\ s$ [4].

The short-side vertical walls of the container were constructed of 20 mm, thick acrylic, and the long-side walls were constructed of either polished acrylic or clear fused quartz. Both the acrylic and fused quartz produced relatively insulative and conductive sidewalls, respectively. The fused quartz sidewalls were used so as to enhance viewing during flow visualization. An air layer depth of $d = 20$ mm was used in most experiments. A range of short-side walls varying from 60 mm in length to 120 mm enabled the secondary aspect ratio, w/d, to be varied. By varying the length of the spacers, we were able to produce experiments in containers at fixed L/d and with parameters w/d ($d < w < L$).

4. EXPERIMENTAL METHOD

A dimensional analysis of the heat transfer problem concerning Rayleigh–Bénard experiments in large containers shows that the heat transport is dependent on the dimensionless Rayleigh number, Ra, which describes the strength in buoyant potential, and the wavenumber, a, which describes the principal length

scale of the roll pattern. The heat transfer can be represented in functional form as [8]

$$N = N(Ra, a) \tag{1}$$

where the normalised dimensionless heat transfer is defined as

$$N = (Nu - 1)\frac{Ra}{Ra_c}. \tag{2}$$

In equation (2) the Nusselt number is defined by the traditional form [10]

$$Nu = \frac{q_{conv}}{q_{cond}} \tag{3}$$

where q_{cond} represents the conductive heat transfer which would occur at ΔT_c, and q_{conv} the convective heat transfer as induced by the same temperature difference. Alternate definitions for representing the heat transfer are, of course, available. The form for N in terms of Ra/Ra_c produces a linear function in the depiction of theoretical and experimental results in extended geometry. Use of the Nusselt number, Nu, in terms of Ra/Ra_c gives the traditional appearance of a quadratic function for the pitchfork bifurcation.

Properties of air in the experiments were defined simply as follows. Kinematic viscosity, ν, is dependent upon laboratory ambient pressure as

$$\nu = \frac{\mu}{\rho} \tag{4}$$

and $\rho = P/RT_m$ is approximated as an ideal gas at low pressure since the compressibility factor for air at 20°C, 1.0 atm is unity [11]. Since the experiments proceed at constant mean temperature $T_m = (T_{upper} + T_{lower})/2 = \text{constant}$, the absolute viscosity, μ, is constant and the coefficient of volume expansion

$$\beta = \frac{1}{\rho}\left(\frac{\partial \rho}{\partial T}\right)_P = \frac{1}{T_m} \tag{5}$$

also remains constant, for the ideal gas model [11]. The density, ρ, is estimated in terms of the laboratory ambient pressure and mean cell temperature T_m. Laboratory ambient pressure was determined from a US Signal Corp-type room barometer with measurements taken at the beginning and end of the experiments. The error in local pressure measurements as compared to Weather Bureau pressure are within $\pm 0.6\%$ [4, 8].

The wavenumber is defined as [12]

$$a = \frac{2\pi d}{\lambda} \tag{6}$$

where the wavelength, λ, is taken as the width of a roll pair. At convective onset, $Ra = Ra_c$, the flow structure is comprised of essentially square rolls of approximately the same width as height, so $a_c \simeq \pi$. Linear stability theory [13] gives the convective onset values $(Ra, a)_c = (1707.8, 3.117)$ for an extended system. By choosing containers which have integer long-side dimensions, $a_c = \pi$ is normally observed in the experiments, but Ra_c is geometry dependent [6, 14, 15]. Consequently, for moderate size containers, the wavenumber has a more complex relationship [6].

$$a = a(Ra, Pr, L/d, w/d, \text{initial conditions}) \tag{7}$$

where L/d and w/d represent the normalised length and width of the container. In equation (7) Pr is the Prandtl number and signifies the fluid under consideration. In these experiments air was the working fluid with $Pr \simeq 0.7$, which is essentially a constant over the heating ranges of these experiments. The initial state of the test apparatus, air layer and laboratory environment, was one of thermal and mechanical equilibrium in terms of temperature and pressure.

Starting experiments systematically from this initial state provided, to a great extent, control over the initial conditions. In lieu of the above, equation (2) can be represented as

$$N = N(Ra, a, L/d, w/d) \tag{8}$$

with the implied condition $a = a(Ra, L/d, w/d)$ [8].

In experiments, the convective heat flux at the test apparatus centerline, co-parallel to the long sidewalls, was evaluated using equation (3) as [6, 13–19]

$$Nu_i = \left(\frac{q_{conv}}{q_{cond}}\right)_i = \left(\frac{V}{V_{cond}}\right)_i = \left(\frac{V}{A + B\Delta T_c}\right)_i \tag{9}$$

for each heat flux gauge, i, in which V_i is the voltage produced in response to the cell temperature difference ΔT_c. $V_{cond,i}$ is the expected value for conduction heat transfer at the same temperature difference, ΔT_c and A, B are linear regression constants determined from least-squares fit of the $V - \Delta T_c$ characteristic of the conduction range of a convection experiment ($Ra < 1708$ for the larger containers).

The temperature difference across the layer was determined from two 36-gauge copper–constantan thermocouples attached to each aluminum sheet and from a differential thermocouple with thermojunctions also attached to the aluminum sheets at the horizontal center of the apparatus [4, 16]. The thin-film heat flux gauges were fabricated from 25 mm thick copper and nickel foils, silver-soldered to form thermojunctions at either horizontal surface of a balsa substrate. Placement of the heat flux gauges in the apparatus resulted in local heat flux measurements at the central vertical plane of the test cell, so that the measurements obtained corresponded to conditions at the cross-section of the convection rolls in the parallel-roll flow configuration.

Convective heat flux at the test apparatus centerline co-parallel to the long sidewalls was evaluated simply as

$$Nu_i = \left(\frac{q_{conv}}{q_{cond}}\right)_i = \left(\frac{V}{V_{cond}}\right)_i \tag{10}$$

for each heat flux gauge, i, in which V is the voltage produced at cell temperature difference ΔT and V_{cond} is the expected voltage for conduction heat transfer at the same temperature difference. To determine whether equation (11) gives an accurate estimate of the heat transfer, we physically turned the apparatus upside down to investigate the performance of the instrumentation at similar heating and cooling rates as those used in the convective heat flux measurement experiments. The constant temperature bath/recirculators were operated in linear programs in these experiments and this produced conduction experiments at the same heat flux gauge temperatures as used for convective heat flux measurements.

Figure 3 shows the efficiency of extrapolated linear least-squares curve fit of data for one of the heat flux gauges. The curve fit range assumed for each experiment is $0.2 < \Delta T_c < 3.28°C$, with the upper limit as the requisite cell temperature difference to produce the average conditions at 0.86 atm and mean temperature of 23°C for convective onset in experiments with the $10 \times 4 \times 1$ configuration ($Ra_c = 1850$ [4, 6]). The extrapolated range in Fig. 3 is consequently over five times larger than that used to produce the linear least-squares curve fit. The experimental data shown in Fig. 3 are taken at equal increments of the cell temperature difference, and as illustrated, the efficiency reaches optimum performance for heating periods $H \geqslant 180$ min. Indeed,

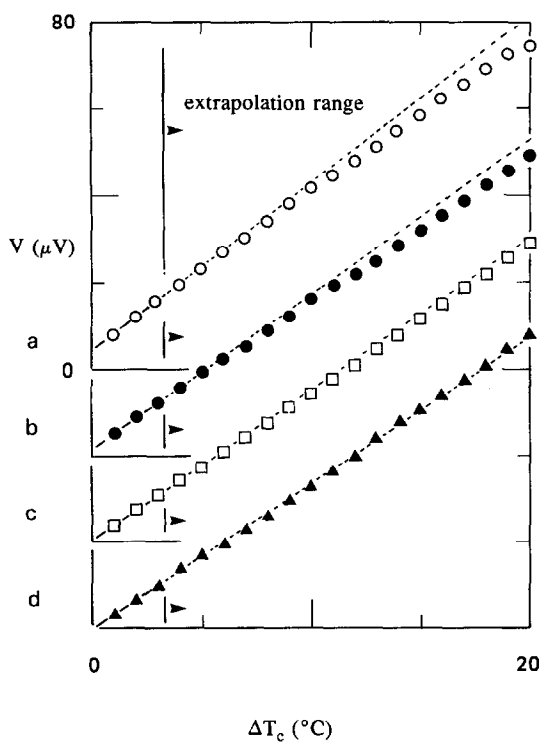

Fig. 3. Efficiency of least-squares fit of conduction range, $0.2°C < \Delta T < 3.28°C$. Dotted lines are extrapolated linear functions. Heating period, H = (a) 2 h, (b) 3 h, (c) 4 h, (d) 5 h.

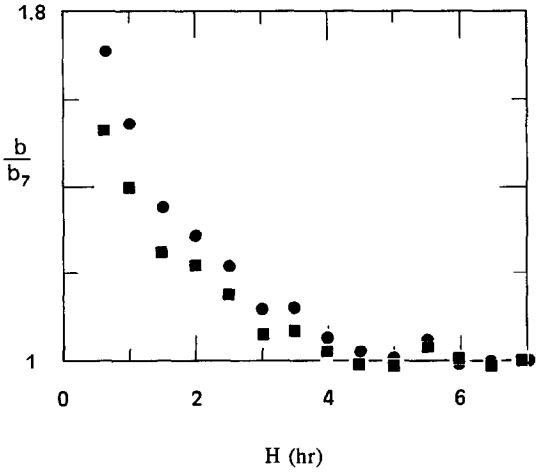

Fig. 4. Asymptotic behavior of conduction range slope: ● inner gauges; ■ outer gauges; b_7 is the slope of linear least-squares fit for $H = 7$ h.

Fig. 4 shows the behavior of the slope of the linear curve fit, b (in $V = a + b\Delta T$) as a function of heating period, such that the best available accuracy of measurement is achieved for heating periods in excess of about 180 min. This corresponds to a maximum rate of increase of the Rayleigh number of approximately 0.93 s^{-1}.

5. RESULTS AND DISCUSSION

Heat flux measurement results were obtained from a series of experiments as described above, with excursion times of 180–240 min to similar steady states. Whereas the voltage produced by the thermoelectric/resistive heat flux gauges is a reliable measure of local heat flux, the measurement of heat flux is quite sensitive to heat transfer through the acrylic sidewalls. This is not surprising, noting that the ratio of sidewall area to heat transfer surface area for a $10 \times 4 \times 1$ geometry is 0.7. The heat flux data reported here are comprised of experimental heat flux results from a series of approximately 60 experiments, with those for which the heat transfer interaction with the environment at the sidewalls is negligible. By ensuring that the mean cell temperature did not deviate by more than $\pm 0.05°C$ from that of the laboratory environment, a net adiabatic condition was maintained between the test cell and laboratory ambient.

The heat flux growth for containers with normalised long sidewalls in the range $8 \leqslant L/d \leqslant 16$ will be discussed first in terms of normalised heat flux, $N = (Nu - 1)Ra/Ra_c$ vs Ra/Ra_c, where Ra_c is the corresponding critical Rayleigh number for each particular geometry. In these figures, the first flag represents convective onset. Subsequent flags represent changes in the heat flux, as induced by secondary bifurcations in the flow structure. Wavenumber selection in the experiments has been discussed previously [4, 19], and a summary of the results is included in Table 1 for reference. As noted in Table 1 and in the discussion which follows,

Table 1. Summary of bifurcation Rayleigh numbers [4, 19]

		$8\times3\times1$	$10\times4\times1$	$12\times4\times1$	$14\times4\times1$	$16\times6\times1$
Convective onset	Ra_c	1880	1850	1800	1780	1730
Single-roll loss	Ra_1	7620	2390	2550	4270	2170
	Ra_2	9600	6620	5770	5130	3450
	Ra_3	—	10 880	9160	—	—
Roll-pair loss	Ra_1	9300	4620	4040	4730	—
	Ra_2	12 500	6860	5540	—	—
	Ra_3	—	11 400	9650	—	—

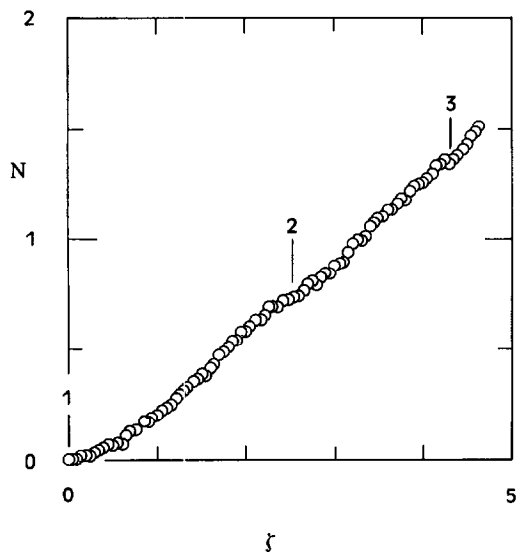

Fig. 5. Heat flux growth in experiments with $8\times3\times1$ configuration: (1) onset of convection at $Ra/Ra_c = 1$ ($Ra_c = 1880$); subsequent bifurcations to (2) seven rolls; (3) six rolls.

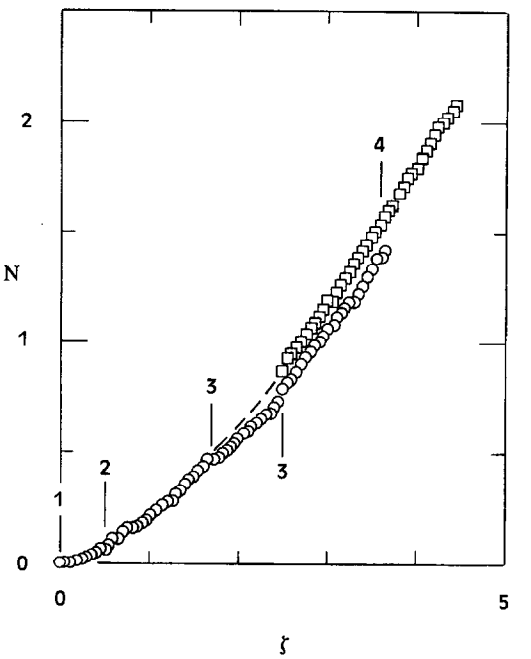

Fig. 6. Heat flux growth in experiments with $10\times4\times1$ configuration. (1) onset of convection ($Ra_c = 1850$), upper branch; (2) $10r$–$9r$ bifurcation; (3) $9r$–$8r$ bifurcation; (4) $8r$–$7r$ bifurcation. Lower branch: (3) $10r$–$8r$ two-step roll-pair bifurcation [16].

each container geometry exhibits two distinct sequences of secondary bifurcation.

Average heat flux determined in the $8\times3\times1$ container is represented in Fig. 5. Convective onset is characterized by flag 1, and occurred at a Rayleigh number of $Ra = 1880$. Following onset, the normalized heat flux exhibits a slight quadratic growth (an issue to be discussed shortly), up to the first secondary bifurcation, flag 2, which represents the eight roll–seven roll transition at a Rayleigh number of $Ra = 6580$. The growth in the heat flux exhibits that of a linear growth for the seven roll configuration where [4]

$$\left.\frac{dN}{d(Ra/Ra_c)}\right|_{Ra=8020} = 0.24\pm0.02. \qquad (11)$$

The slope of the growth rate are determined by linear least-squares fit of the data (36 points) between flags 2 and 3. Flag 3, Fig. 5, denotes the bifurcation from seven to six rolls. The experiment terminated at a steady state Rayleigh number of 10 200.

The average heat flux measured in the $10\times4\times1$ container is illustrated in Fig. 6. The upper branch (including the extrapolated portion) represents a sequence of single-roll loss bifurcations, whereas the lower branch exhibits a roll-pair loss bifurcation. This container size and shape is the only geometry studied for which we can clearly distinguish the single-roll and two-step roll-pair loss bifurcation sequences in heat flux measurement. Flag 1 indicates the onset of convection, which occurs at an average Rayleigh number of 1850. An extrapolation of the upper branch is shown in Fig. 6, as the heat flux data in that region is outside the ±0.05°C bounds set by the experimental method (see Fig. 2). For the upper branch, flag 2 indicates the 10 roll–nine roll transition ($Ra = 2400$), flag 3 the nine roll–eight roll transition, and flag 4 the eight roll–seven roll transition. The lower branch represents heat flux measurements generated from experiments exhibiting the two-step roll-pair loss

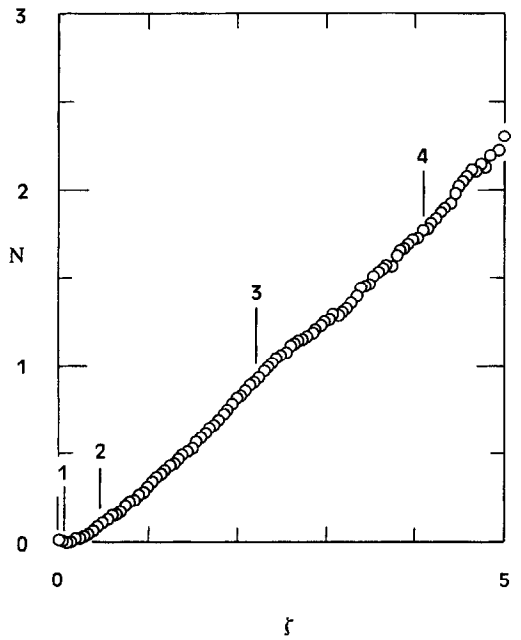

Fig. 7. Heat flux growth in experiments with $12 \times 4 \times 1$ configuration. (1) convective onset ($Ra_c = 1870$); (2) $12r$–$11r$ bifurcation; (3) $11r$–$10r$ bifurcation; and (4) $10r$–$9r$ bifurcation. Terminal $Ra = 10\,800$.

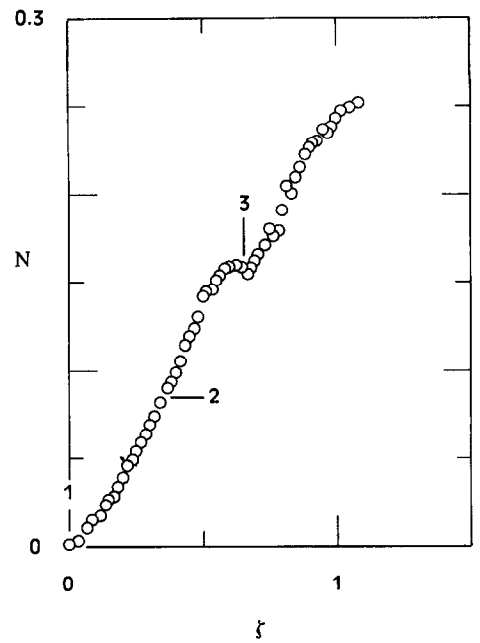

Fig. 8. Heat flux growth in experiments with $14 \times 5 \times 1$ configuration. (1) convective onset ($Ra_c = 1780$); (2) $14r$–$13r$ bifurcation; (3) $13r$–$12r$ bifurcation. Terminal $Ra = 5540$.

bifurcation sequence. The 10 roll–eight roll transition is noted by flag 3 in the lower branch in Fig. 6.

Figure 7 shows the average heat flux determined from experiments in the $12 \times 4 \times 1$ container. Onset occurs at $Ra = 1870$, as flagged by 1 in Fig. 7. The 12 roll–11 roll transition, flag 2, is soft, but as confirmed by time–voltage signature traces of the experiment occurs at $Ra = 2600$. The mild change of slope is characterised by a gradual contraction of the wall roll created by the climbing dislocation. The second secondary bifurcation, that to 10 rolls, produces a stronger discontinuity in the heat flux data, and is due to the higher convective propagation speed. An independent smoke flow visualization experiment revealed a stable 11-roll flow structure in the range $Ra = 2600$–5700 (i.e. between flags 2 and 3). The third secondary bifurcation, denoted by flag 4, illustrates the transition to nine rolls.

Figure 8 shows the average heat flux determined from experiments in the $14 \times 5 \times 1$ container. Onset occurs at $Ra = 1780$ and is depicted by 1. The 14 roll–13 roll single-roll transition, flag 2, is *soft* an is characterised by the gradual contraction of the wall roll. Flag 3 indicates the 13–12 transition and reveals a stronger discontinuity in the heat flux. Comparison of the heat flux characteristics in the $14 \times 5 \times 1$ container with the smaller containers reveals a more linear growth in the convective heat flux.

The last geometry studied with regard to heat flux measurements is the $16 \times 6 \times 1$ container, and is shown in Fig. 9. Onset occurred at $Ra = 1730$ and is depicted by flag 1. Close inspection of the onset condition

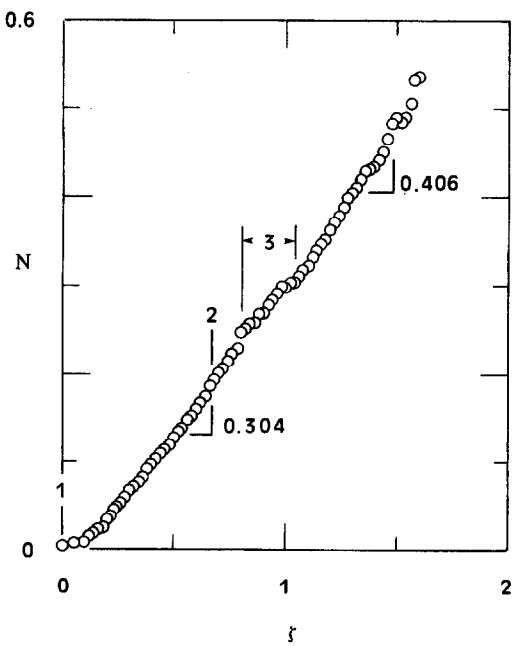

Fig. 9. Heat flux growth in experiments with $16 \times 6 \times 1$ configuration. (1) convective onset ($Ra_c = 1730$); (2) $16r$–$15r$ bifurcation; (3) $15r$–$14r$ bifurcation. Terminal $Ra = 5500$.

reveals a transition to a linear growth in heat flux with [4]

$$\left.\frac{dN}{d(Ra/Ra_c)}\right|_{Ra=Ra_c} = 0.304 \pm 0.025. \qquad (12)$$

The bifurcation from 16 to 15 rolls is represented by

2, and is soft. The 15–14 bifurcation, 3, occurred over a range of normalised Rayleigh number, $1.7 \leqslant Ra \leqslant 1.9$. After the 14-roll pattern has stabilised, the normalised heat flux reveals a linear growth as [4]

$$\frac{dN}{d(Ra/Ra_c)}_{2Ra>Ra_c} = 0.406 \pm 0.180. \quad (13)$$

The trend towards linear growth in the normalised heat flux is exhibited in Figs 8 and 9 and is consistent with the theoretical predictions of Schlüter *et al.* [20] for extended systems. The characteristics of nonlinear growth in the small, moderate-size containers with the relaxation to linear growth in larger, moderate-size contains for onset conditions is exploited next.

5.1. *Near convective onset heat transfer characteristics*

The heat flux in the eight-roll configuration is illustrated in Fig. 10, the curve fit for which can also be described in terms of a quadratic function. The y-intercept is identically zero, $N(0) = 0$, by regression analysis in the form

$$\frac{N}{\zeta} = a + b\zeta \quad (14)$$

where $\zeta = Ra/Ra_c - 1$. Thus, equation (14), with two terms as

$$N = a\zeta + b\zeta^2 \quad (15)$$

gives the leading order representation of experiments. The regression analysis produced the near onset growth as $N = 0.066\zeta + 0.118\zeta^2$ [4].

The near onset growth in heat flux in the 10-roll configuration is illustrated in Fig. 11. Here, the regression analysis produced the growth as, $N = 0.089\zeta + 0.12\zeta^2$ [4]. As in the eight-roll onset behavior just discussed, the heat flux growth in the 10-roll configuration is well represented by the regression, and exhibits a strong quadratic growth. Our understanding at this time is that the quadratic growth is due to imperfections induced by the presence of the sidewalls, as discussed below.

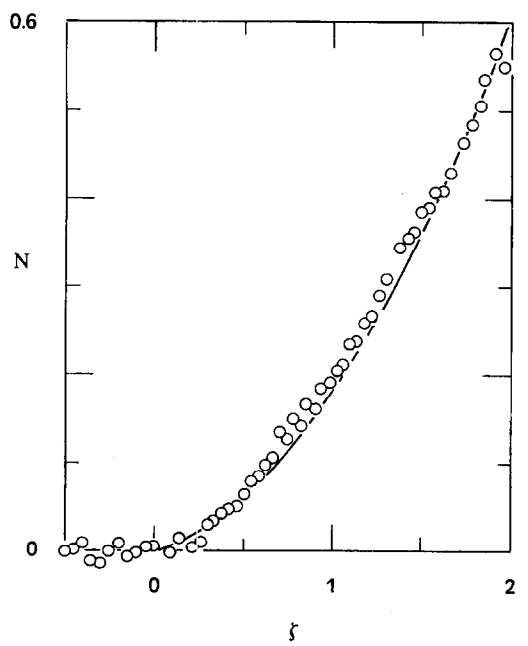

Fig. 10. Quadratic growth of heat flux near onset, eight-roll, configuration ($8 \times 3 \times 1$ geometry). $N = 0.066\zeta + 0.118\zeta^2$.

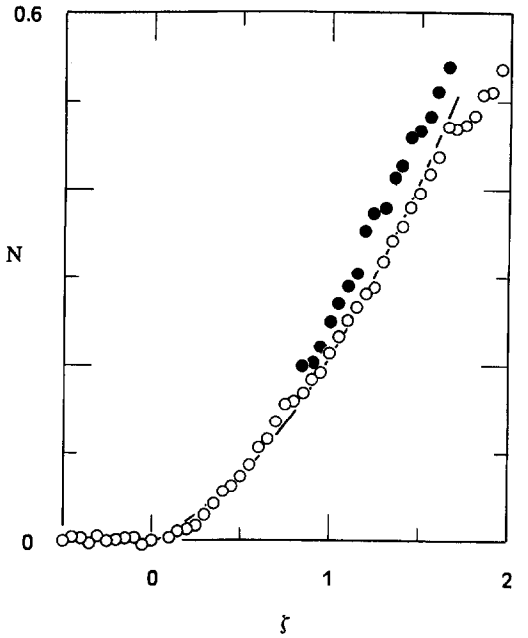

Fig. 11. Quadratic growth of heat flux near onset, ten-roll, configuration ($10 \times 4 \times 1$ geometry). $N = 0.089\zeta + 0.12\zeta^2$ for the lower bifurcation sequence (○).

The near onset growth in heat flux in the 12-roll configuration is illustrated in Fig. 12. Regression analysis produced a growth as, $N = 0.104\zeta + 0.0189\zeta^2$ [4] Inspection of the near onset growth reveals a slight flattening (i.e. a trend towards linear growth) in the curve, and that the coefficients characterising the growth are of comparable magnitude. Initiation of the secondary bifurcation structure at $Ra = 2600$ is clearly evident in Fig. 12.

Figures 13 and 14 illustrate the near onset heat flux behavior in the $14 \times 5 \times 1$ and $16 \times 6 \times 1$ containers, and exploit the relaxation in quadratic growth of the heat flux. Regression analysis of the $14 \times 5 \times 1$ and $16 \times 6 \times 1$ for the near onset heat flux regime produced $N = 0.155\zeta + 0.211\zeta^2$ and $0.308\zeta + 0.033\zeta^2$, respectively [4]. Figure 14 certainly reveals the relaxation in quadratic growth as compared to the smaller, moderate-size containers since the linear coefficient is a factor of 10 larger than the quadratic coefficient. Consequently, the approach to linear growth for containers with increasing longside dimension, as exploited here, is more evidence of the demarcation between the moderate and larger container regimes. A summary of the near onset growth rate behavior in

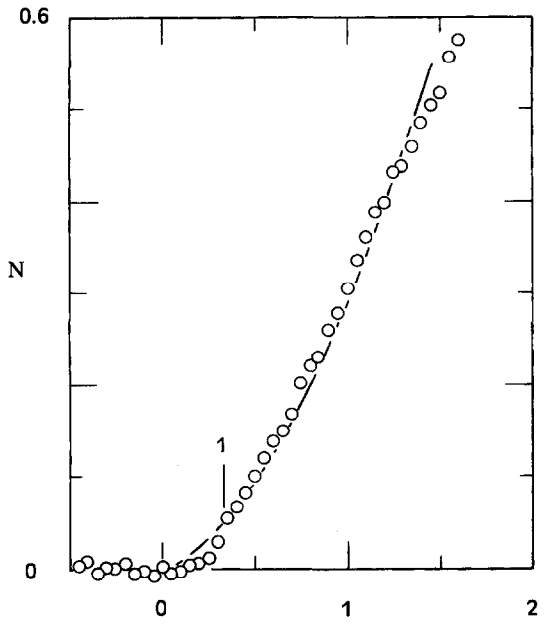

Fig. 12. Quadratic growth of heat flux near onset, twelve-roll, configuration ($12\times4\times1$ geometry), $N = 0.104\zeta + 0.189\zeta^2$. Flag 1 shows the bifurcation to an 11-roll flow structure.

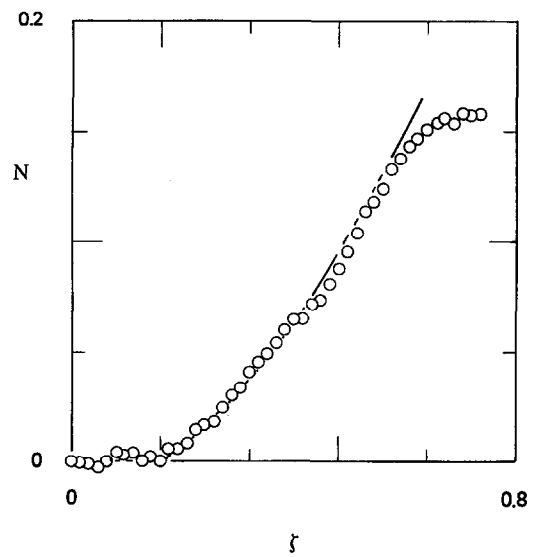

Fig. 13. Quadratic growth of heat flux near onset, 14-roll, configuration ($14\times5\times1$ geometry). $N = 0.155\zeta + 0.211\zeta^2$.

the containers $L/d = 8$–16 are presented in Table 2 [4].

5.2. *Imperfection of bifurcation in the experiments*

The observed quadratic dependence of the heat flux on Rayleigh number is attributed to imperfections manifested in the experiments. *Imperfect bifurcation* is not only a physical realization in many experimental situations, but is indeed expected in the experiments which we report here. Adiabatic sidewalls are required to produce *simple* models of the convection, and these

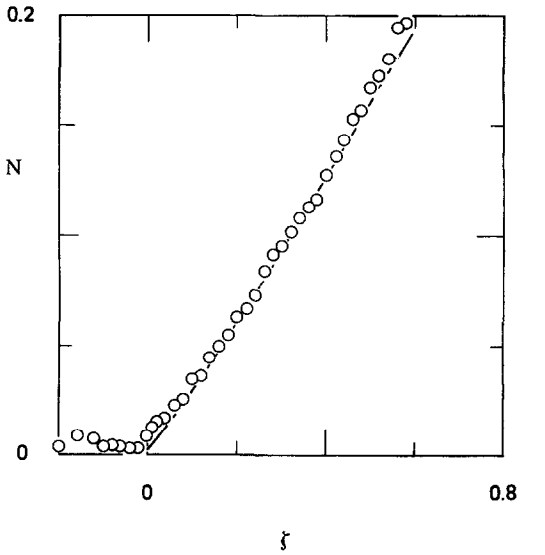

Fig. 14. Quadratic growth of heat flux near onset, 16-roll, configuration ($16\times6\times1$ geometry). $N = 0.308\zeta + 0.033\zeta^2$.

Table 2. Summary of near onset heat flux growth for $L/d = 8$–16. Tabulated values are the linear ζ and quadratic ζ^2 coefficients, where $N = a\zeta + b\zeta^2$. The corresponding error estimates were computed using the 95% error interval

L/d	a	b
8	0.066 ± 0.042	0.118 ± 0.012
10	0.089 ± 0.016	0.120 ± 0.016
12	0.104 ± 0.043	0.189 ± 0.049
14	0.155 ± 0.091	0.211 ± 0.14
16	0.308 ± 0.01	0.033 ± 0.01

same models, at lowest order, describe the convective onset as a supercritical bifurcation. More specifically, the perfect bifurcation model for convective onset is the pitchfork bifurcation. Our minimum-error experiments are characterized by *net adiabatic conditions* of the test cell with respect to the laboratory environment. Since the sidewalls are constructed of acrylic, there are non-zero heat transfer interactions between the test apparatus and laboratory environment ($q > 0$ near the upper surface and $q < 0$ near the lower surface, with q as the heat transfer from the laboratory ambient to the test cell). We noted earlier that to obtain accurate heat flux measurements ($\pm5\%$ error interval) at the long-side vertical plane of the test cell, it is necessary to maintain a mean cell temperature to within ±0.05°C of the laboratory ambient temperature. While this is difficult to achieve in practice without the use of an environmental chamber, the results reported here are confined to the stated measurement accuracy. Even with net adiabatic conditions, there are heat transfer interactions present and, consequently, all bifurcations manifested in experiments, both primary bifurcation at onset and the hierarchy of secondary bifurcation at wavenumber reduction, are imperfect. Near convective onset (slightly super-

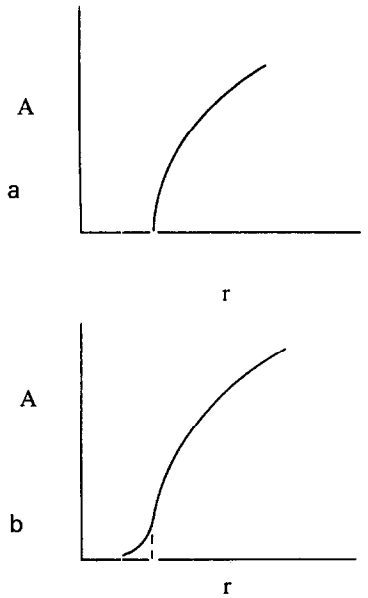

Fig. 15. Imperfection in bifurcation at convective onset. (a) pitchfork bifurcation, (b) imperfect bifurcation.

critical conditions, $Ra > Ra_c$), a dynamical system model can be posed as [21]

$$\frac{dA}{dt} = \phi + rA - A^3 \tag{16}$$

where $r = Ra - Ra_c$, and ϕ represents the imperfection from the equilibrium state ($dA/dt \to 0$). In this sense, both ϕ and r are control parameters. The imperfect bifurcation is illustrated in Fig. 15, and $\phi \to 0$ then produces the perfect pitchfork bifurcation at equilibrium.

Finally, a second source of imperfection is present in some experiments, and is manifested as a local formation of an initial convection roll at one short sidewall and *followed* by formation of a convection roll at the opposite short sidewall. The interior pattern subsequently forms to produce the system of rolls which characterise onset. Then a variation of the one-dimensional Ginzburg–Landau equation, or alternately the Newell–Whitehead–Segel equation is suggested as

$$\frac{\partial A}{\partial t} = \phi + rA - A^3 + \xi \frac{\partial^2 A}{\partial x^2} \tag{17}$$

with ξ as a coherence length scale. The problem with equation (17) in accounting for non-equilibrium behavior is that only one sidewall is considered. A left- and right-running amplitude are then needed to model the *two* short sidewalls (the far-field condition cannot be enforced at $x = L/2$), and also the long sidewalls produce strong modulation of convection rolls. Since we have only reported experimental behavior in this study, the modeling issue is considered a peripheral concern. Influences of multiple sidewalls have been considered previously by Manneville [22]. Finally, the two-control parameter problem in analysis of imperfect bifurcation has been addressed previously by Ahlers [23] and Hall and Walton [24], and the structural stability in related problems is discussed rather thoroughly by Drazin and Reid [21].

5.3. *Comparison of experimental results with previous results in extended geometry*

We noted earlier that the heat flux measurements for the larger containers considered approach the behavior observed in extended systems. An earlier theoretical result for infinite horizontal layers was posed by Schlüter *et al.* [20] as

$$\frac{Nu-1}{(Ra/Ra_c)-1} = \frac{1}{0.69942 - 0.00472/Pr + 0.00832/Pr^2} \tag{18}$$

for convection rolls near onset. With $Pr = 0.7$, this gives $N = 1.409\zeta$ in the notation used here. This result compares favorably with the correlation of experimental results reported by Hollands *et al.* [25]

$$Nu = 1.44\left(\frac{Ra}{Ra_c} - 1\right), \quad 1708 < Ra < 5830 \tag{19}$$

or $N = 1.44\zeta$.

In cylindrical containers of helium and diameter to depth ratio of $D/d = 10$, Ahlers [23] determined the near-onset heat flux as $N = 0.84\zeta$ for stable roll patterns and $N = 0.56\zeta$ for unstable patterns. The slope in $N-\zeta$ coordinates is small for heat flux measurements in the moderate size containers considered here, but the experimental observations for increased container size clearly approach the expected linear behavior for wide layers. We note again that our heat flux measurements are not average values over the planform of the pattern, but represent only the average heat flux at the midplane of the pattern and coparallel to the long sidewalls.

6. CONCLUSIONS

The nonlinear dynamical behavior in finite Rayleigh–Bénard convection can be described qualitatively in terms of the initial growth rate in the heat flux. The Ginzburg–Landau equation, or Newell–Whitehead–Segel equation predicts the convective onset as a supercritical bifurcation, in analogy with a second-order phase transition, and the initial growth rate of heat flux at low Rayleigh number. The results presented here are in excellent agreement with previous experimental work in wide-layers with gases and cryogens. However the new results reported here for experiments in moderate size containers appear to depart from the wide-layer results in a manner which can be expressed as a quadratic growth in the heat flux. Heat flux results in the large containers shows a relaxation in the quadratic growth to that of a linear

growth which is consistent with the theoretical predictions of heat flux in extended systems. This is an important result since all numerical results, and most experimental results dealing with air have been performed in extended systems. Although the quadratic growth in heat flux has been a point of contention by some investigators, this study exploits the behavior, and moreover is backed by precise uncertainty calculations.

REFERENCES

1. Normand, C., Pomeau, Y. and Velarde, M. G., Convective instability: a physicists's approach. *Review of Modern Physics*, 1977, **49,** 581–624.
2. Busse, F. H., Nonlinear properties of thermal convection. *Rep. Progress in Physics*, 1978, **141,** 1929–1967.
3. Leith, J. R., Flow structure transitions in Rayleigh–Bénard convection of air in rectangular containers. *8th Annual Conference, Center for Nonlinear Studies*, Los Alamos National Laboratory, 1988.
4. Maveety, J. G., Bifurcation dynamics in thermal convection. Ph.D. thesis, University of New Mexico, 1994.
5. Leith, J. R., Successive transition of steady states in moderate size containers of air heated below and cooled above. In *Bifurcation Phenomena in Thermal Processes and Convection*, ASME HTD-94/AMD-89, eds H. H. Bau, L. A. Bertram, and S. A. Korpela. ASME, New York, 1987, pp. 91–98.
6. Leith, J. R., Flow structure transition mechanism in thermal convection of air in rectangular containers. *Physica D*, 1989, **37,** 334–340.
7. Hager, N. E., Thin foil heat meter. *Review of Science Instruments*, 1965, **36,** 1564–1570.
8. Leith, J. R. and Maveety, J. G., Investigation of the thermoelectric/resistive behavior of thin-film heat flux gauges. *Thermal Fluid Science*, 1996 (submitted).
9. Özisik, M. N., *Heat Conduction*, 2nd edn. Wiley, New York 1993.
10. Chandrasekhar, S., *Hydrodynamic and Hydromagnetic Stability*. Dover Publications, 1981.
11. Callen, H. B., *Thermodynamics and an Introduction to Thermostatistics*, 2nd edn. Wiley, New York, 1985.
12. Platten, J. K. and Legros, J. C., *Convection in Liquids*. Springer, Berlin, 1984.
13. Reid, W. H. and Harris, D. L., Some further results on the Bénard problem. *Physics of Fluids*, 1958, **1,** 102–110.
14. Leith, J. R., Suppression of flow structure dislocations in thermal convection experiments. *Experimental Fluids*, 1989, **7,** 427–428.
15. Maveety, J. G. and Leith, J. R., Heat flux at secondary bifurcation in Rayleigh–Bénard convection with air in a rectangular container. *International Communication of Mass Transfer*, 1991, **18,** 59–70.
16. Leith, J. R. and Maveety, J. G., Modeling of bifurcation in Rayleigh–Bénard convection with air in rectangular containers. In *Bifurcation Phenomena and Chaos in Thermal Convection*, eds H. H. Bau, L. A. Bertram and S. A. Korpela. ASME HTD-Vol. 214/AMD-Vol. 138, 1992, pp. 99–109.
17. Leith, J. R. and Maveety, J. G., Bifurcation in Rayleigh–Bénard convection with gases in rectangular containers. In *Integral Methods in Science and Engineering*—90, eds A. Haji-Sheikh, C. Corduneanu, J. L. Fry, T. Huang and F. R. Payne. Hemisphere, New York, 1991, pp. 376–387.
18. Maveety, J. G., Convective heat flux measurements of air in rectangular Rayleigh–Bénard cells. M.S. thesis, University of New Mexico, 1990.
19. Leith, J. R. and Maveety, J. G., Wavenumber evolution in Rayleigh–Bénard convection with air in moderate size containers. *International Communication of Heat and Mass Transfer*, 1994, **21,** 237–248.
20. Schlüter, A., Lortz, D. and Busse, F., On the stability of steady finite amplitude convection. *Journal of Fluid Mechanics*, 1965, **23,** 129–144.
21. Drazin, P. G. and Reid, W. H., *Hydrodynamic Stability*. Cambridge University Press, Cambridge, 1981.
22. Manneville, P., *Dissipative Structures and Weak Turbulence*. Academic Press, New York, 1990.
23. Ahlers, G., Low-temperature studies of the Rayleigh–Bénard instability and turbulence. *Physics Review Letters*, 1974, **33,** 1185–1188.
24. Hall, P. and Walton, I. C., Bénard convection in a finite box: secondary and imperfect bifurcations. *Journal of Fluid Mechanics*, 1979, **90,** 377–395.
25. Hollands, K. G. T., Raithby, G. D. and Konicek, L., Correlation equations for free convection heat transfer in horizontal layers of air and water. *International Journal of Heat and Mass Transfer*, 1975, **18,** 879–884.